JOURNAL OF GEOPHYSICAL RESEARCH, VOL. 106, NO. B7, PAGES 13,565–13,580, JULY 10, 2001

Spatial extent of a hydrothermal system at Kilauea Volcano, Hawaii, determined from array analyses of shallow long-period seismicity 1. Method

Javier Almendros, Bernard Chouet, and Phillip Dawson
U.S. Geological Survey, Menlo Park, California

Abstract. We present a probabilistic method to locate the source of seismic events using seismic antennas. The method is based on a comparison of the event azimuths and slownesses derived from frequency-slowness analyses of array data, with a slowness vector model. Several slowness vector models are considered including both homogeneous and horizontally layered half-spaces and also a more complex medium representing the actual topography and three-dimensional velocity structure of the region under study. In this latter model the slowness vector is obtained from frequency-slowness analyses of synthetic signals. These signals are generated using the finite difference method and include the effects of topography and velocity structure to reproduce as closely as possible the behavior of the observed wave fields. A comparison of these results with those obtained with a homogeneous half-space demonstrates the importance of structural and topographic effects, which, if ignored, lead to a bias in the source location. We use synthetic seismograms to test the accuracy and stability of the method and to investigate the effect of our choice of probability distributions. We conclude that this location method can provide the source position of shallow events within a complex volcanic structure such as Kilauea Volcano with an error of ± 200 m.

1. Introduction

The classic approach to locate a seismic event requires a determination of the arrival times of several phases at different stations in a distributed network. The more precise this determination, the more constrained the source location. The arrival times are inverted to obtain a minimum error solution for the event coordinates and origin time, using velocity information from a seismic model, usually in the form of a layered half-space.

An alternate to the classic method is the use of seismic antennas to determine the source location. A seismic antenna provides a vector, named the slowness vector, which represents the propagation properties (direction and apparent velocity) of the wave fronts across the antenna. The source coordinates are then obtained by inverting the slowness vector information from multiple synchronized antennas within the framework of a seismic velocity model.

Accurate location of long-period (LP) seismicity in volcanoes [*Chouet*, 1996a] has been a major issue for seismologists since the first deployment of seismometers on a volcano. LP seismicity encompasses both discrete LP events and tremor. LP events are usually characterized by an emergent onset and a lack of clear *S* phases, while tremor is a sustained signal with no readily identifiable phases. This lack of distinct phases makes it difficult to locate LP seismicity with the conventional phase pick method, especially when dealing with shallow sources. On rare occasions, LP events are impulsive enough to enable the application of the classic location procedure; however, the associated location uncertainties are usually quite large [*Koyanagi et al*., 1987; *Lahr et al*., 1994].

As array techniques do not rely on phase picks, antennas are particularly useful when dealing with LP seismicity and may in fact constitute the only means to obtain precise source locations for LP sources. Several attempts have been made to locate LP sources using information from slowness vectors provided by seismic antennas. When only one antenna is available, the usual method for obtaining the source position is to assume the epicentral distance (for example, by assuming that the source is located vertically beneath a surface feature, such as an active vent, in the direction indicated by the back azimuth). The depth is then estimated by applying a ray-tracing procedure [*Goldstein and Chouet*, 1994; *Chouet et al*., 1997; *Ibáñez et al*., 2000]. The use of a circular wave front geometry may also provide an estimation of the epicentral distance [*Almendros et al*., 1999]. However, the combined information from several antennas remains the best way to determine simultaneously the epicentral distance and hypocentral depth [*Bratt and Bache*, 1988; *Métaxian et al*., 1997; *Almendros et al*., 2000; *La Rocca et al*., 2000]. In this paper, we present a probabilistic method that uses slowness vector data derived from frequency-slowness analyses of array data from at least two seismic antennas to determine the source location of a seismic event.

Paper number 2001JB000310.
0148-0227/01/2001JB000310$09.00

2. Frequency-Slowness Method

Many methods are available in the literature to extract information on the slowness vector from seismic array data, such as conventional or high-resolution beam forming [*Capon*, 1969; *LaCoss et al*., 1969] or the cross-correlation method [*Frankel et al*., 1991; *Del Pezzo et al*., 1997; *Almendros et al*.,

1999]. In this paper, we use the MUSIC algorithm [*Schmidt*, 1986; *Goldstein and Archuleta*, 1987, 1991]. This method provides an estimate of the frequency-slowness power spectrum with the advantages of high-resolution capabilities and short computation time.

The MUSIC method performs an eigendecomposition of the cross-spectral matrix of the seismograms recorded at a seismic antenna, focused at a frequency f within a given frequency interval [*Wang and Kaveh*, 1985]. Eigenvectors corresponding to the large eigenvalues determine the signal subspace, whereas the remaining eigenvectors determine the noise subspace. Solutions are sought by projecting a generic array response vector that contains information about the spatial dependence of the phase of a plane wave crossing the array, over the noise subspace. Signals provide minimum projections and thus can be determined by the maxima of a function $D(f, \mathbf{s})$, called the frequency-slowness power spectrum and defined as

$$D(f, \mathbf{s}) = \left(\sum_{n \in \text{noise}} |\mathbf{B}(f, \mathbf{s}) \cdot \mathbf{v}_n|^2 \right)^{-1}, \tag{1}$$

where $\mathbf{v}_n$ are the eigenvectors representing the noise subspace and $\mathbf{B}$ is the array response vector given by

$$B_j(f, \mathbf{s}) = \exp(i2\pi f \mathbf{s} \cdot \mathbf{r}_j) \tag{2}$$

in which $\mathbf{r}_j$ is the position of station j and $\mathbf{s}$ represent the apparent slowness vector.

A more robust estimation of the slowness of the wave field is obtained by stacking the frequency-slowness power spectra corresponding to a set of focusing frequencies within the band of interest [*Spudich and Oppenheimer*, 1986]. This technique enhances the stable peaks and minimizes the effect of spurious peaks. The stacked slowness power spectrum is obtained as

$$\bar{D}(\mathbf{s}) = \sum_{k \in \text{band}} D(f_k, \mathbf{s}). \tag{3}$$

The apparent slowness vector $\mathbf{s}_0$ corresponding to the dominant peak in the stacked slowness power spectrum, $\bar{D}_0 = \bar{D}(\mathbf{s}_0)$, represents our estimate of the apparent slowness vector of the wave field. The vector $\mathbf{s}_0$ is defined by its corresponding polar coordinates, given by the apparent slowness (or ray parameter) s_0 and azimuth ϕ_0:

$$\begin{aligned} s_0 &= \sqrt{s_x^2 + s_y^2}, \\ \phi_0 &= \frac{\pi}{2} - \arctan\left(\frac{s_y}{s_x}\right), \end{aligned} \tag{4}$$

where s_x and s_y are the Cartesian components of the slowness vector, selected in such a way that the x axis is pointing to the east and the y axis is pointing to the north. With this convention, ϕ_0 represents the signal propagation azimuth, measured clockwise from north.

2.1. Error Estimation

To estimate the error in the determination of the slowness vector, we take into account two effects, namely, the finite grid spacing and the width of the spectral peak. If Δs_{grid} represents the grid interval, the associated errors in azimuth and slowness are (Figure 1)

$$\Delta\phi = \arctan\left(\frac{\Delta s_{\text{grid}}}{s_0}\right), \qquad \Delta s = \Delta s_{\text{grid}}. \tag{5}$$

Using a smaller grid spacing could reduce this error, as long as we do not proceed beyond the resolution of the antenna.

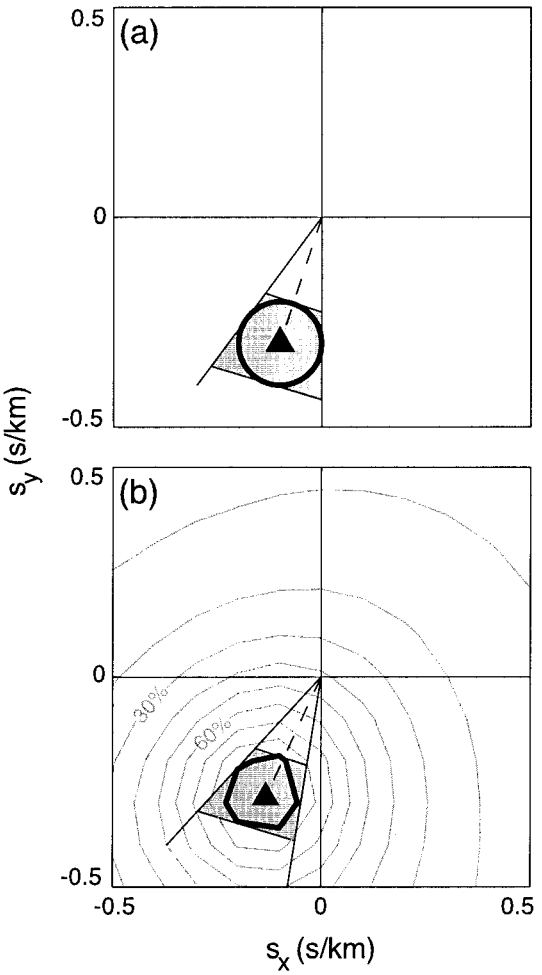

Figure 1. Sketch of the error estimation procedure. (a) Error due to the finite grid spacing. The radius of the bold circle is the grid interval. (b) Error due to the shape of the spectral maximum. The bold contour corresponds to 90% of the maximum. The shaded regions in Figures 1a and 1b define minimum and maximum values for the slowness and azimuth.

The slowness resolution of the antenna, δs, may be estimated from [*Goldstein and Archuleta*, 1991]

$$\delta s = \sqrt{\left(\frac{\delta t}{d\sqrt{N}}\right)^2 + \left(\frac{\sqrt{1+NR}}{2\pi f L N R \sqrt{M}}\right)^2}, \tag{6}$$

where δt is the uncertainty in time delay between stations, d is the average distance between stations, N is the number of stations, R is the signal-to-noise ratio, f is the frequency, L is the array aperture, and M is the number of samples in the analysis window.

However, the error associated with the finite grid spacing does not completely characterize the quality of the solution [*Del Pezzo et al.*, 1997]. We want to know further if the peak we are dealing with is sharp or broad. For this purpose, we consider the size of the region within which the slowness power spectrum is larger than 90% of the maximum value:

$$\begin{aligned} R_\phi &= \{\phi | \bar{D}(\phi, s) > 0.9\bar{D}_0\} \\ R_s &= \{s | \bar{D}(\phi, s) > 0.9\bar{D}_0\}. \end{aligned} \tag{7}$$

This region contains the slowness vector estimation (ϕ_0, s_0) and defines minimum and maximum boundaries for the azimuth and slowness (Figure 1). The total error limits are

$$\begin{aligned} \phi_{\min} &= \min R_\phi - \Delta\phi, \qquad \phi_{\max} = \max R_\phi + \Delta\phi, \\ s_{\min} &= \min R_s - \Delta s, \qquad s_{\max} = \max R_s + \Delta s. \end{aligned} \tag{8}$$

The main source of error is usually the shape of the peak, but the grid spacing becomes important when the peak is very narrow or the apparent slowness of the waves is small.

2.2. Slowness Vector of a Seismic Event

The frequency-slowness analysis of seismic array data provides the values of azimuth and apparent slowness of the wave field, together with the corresponding error limits, as a time series. To obtain an estimate of the slowness vector for direct arrivals from a seismic event, we select a window around the onset of the seismic event. The selection is based on the following properties: (1) the frequency-slowness power is high; (2) the azimuth and slowness are stable; and (3) the errors in both azimuth and slowness estimates are relatively small. We refer to this window as the first-arrival window, even though it may contain not only direct *P* waves but also a mixture of *P* and *S* waves, surface waves, scattered waves, and so on, as long as these waves show coherence across the receivers within the array. We then average the azimuth and slowness values within the first arrival window, using the error as a weighting factor in order to enhance the results with smaller errors. We use weighting functions in the forms $[1 - (\Delta\phi_i/\phi_{\lim})]^n$ and $[1 - (\Delta s_i/s_{\lim})]^n$ for azimuth and slowness, respectively, in which $\Delta\phi_i$ and Δs_i are the errors corresponding to the ith sample, $\phi_{\lim}$ and $s_{\lim}$ are the maximum expected errors, and n is an exponent selected to enhance the difference between the low- and high-error solutions. We select $n = 3$ for our application. The error associated with the average value of either slowness or azimuth is determined as the average of the errors. For the azimuth, which is generally stable within the first arrival window, this is a good estimate of the error. For the apparent slowness, however, we further consider the dispersion of the results, including the error limits, to obtain a better estimate of the range of variation of the solution. This allows us to associate a unique slowness vector to a seismic event observed at a given antenna. The slowness vectors derived from frequency-slowness analyses at separate antennas are used in section 3 to obtain an estimate of the position of the source.

3. Source Location Method

To derive a joint location of the source based on information from multiple seismic antennas, we follow a probabilistic approach that is a simplified version of the statistical method described by *Saccorotti et al*. [1998]. We define a spatial distribution of probability that represents the likelihood of a point of the medium being the source of the seismic event, based on the similarity between the observed slowness vector data and a model.

The frequency-slowness analysis and averaging procedure described in section 2 provide a set of parameters, namely, the apparent slownesses and azimuths, with the corresponding error ranges, observed at different antennas. To ensure that a joint location is successful, we need data from at least two seismic antennas. These data may be summarized as

$$\begin{Bmatrix} \bar{\phi}^A_{\min} & \bar{\phi}^A_0 & \bar{\phi}^A_{\max} \\ \bar{s}^A_{\min} & \bar{s}^A_0 & \bar{s}^A_{\max} \end{Bmatrix}, \qquad A \in \text{arrays}.$$

Let $P^A_\phi(x, y, z)$ be the probability that if the source of the seismic event were located at (x, y, z), the generated waves would propagate through array A with the same azimuth as that determined for the event by experimental analysis. Similarly, $P^A_s(x, y, z)$ is the probability of those waves being detected with the same apparent slowness as that observed for the event. Then the function $\sigma(x, y, z)$, called the spatial source probability and defined as

$$\sigma(x, y, z) = \prod_{A \in \text{arrays}} P^A_\phi(x, y, z)\, P^A_s(x, y, z), \tag{9}$$

represents the probability of point (x, y, z) being the source of the event. We define the source location as the point in the domain where the spatial source probability reaches its maximum and the error limit as the region within the isosurface of 80% of the maximum probability (the selection of this level will be justified a posteriori).

The actual value of the maximum, which we will call location quality (LQ), is a measure of the "goodness" of the solution. LQ is close to 1 when every single probability distribution for azimuth and slowness reaches its maximum at the same point, and their maxima are all close to 1. In that case the source is well constrained. When the maxima are not in the same region, or some of them are small (as seen, for example, when the synthetic slowness at every point differs too much from the observed slowness because the model is not a good representation of the medium), then the maximum of the spatial source probability is also small. This means that the probability distributions for the different parameters are not internally consistent and the resulting uncertainty in the source location is large.

When we consider the source locations for a seismic swarm, we may further sum the spatial probabilities corresponding to all events and produce a stacked spatial probability function that can be used to determine the most active zones in the medium:

$$\bar{\sigma}(x, y, z) = \sum_{i \in \text{events}} \sigma_i(x, y, z). \tag{10}$$

In this sum the spatial source probabilities for individual events are not normalized, and therefore every event is weighted according to its own location quality. The stacked probability may be understood as a map of the seismic activity. This procedure, however, removes all temporal information. If we want to track the source evolution in time, individual locations have to be considered.

To apply (9), we need to define the probability functions $P^A_\phi(x, y, z)$ and $P^A_s(x, y, z)$. Each of these functions must contain a single peak, corresponding to the azimuth and slowness determined for the event, respectively, in order to ensure the uniqueness of the solution. These functions must decay away from the central value and must also be smooth enough to ensure that similar slowness vectors are assigned similar probabilities. Furthermore, the functions must satisfy symmetry restrictions. The probability for azimuth should be symmetric because there is no reason to think that a clockwise direction is to be preferred to a counterclockwise direction. There may be a slight asymmetry caused by the configuration of the

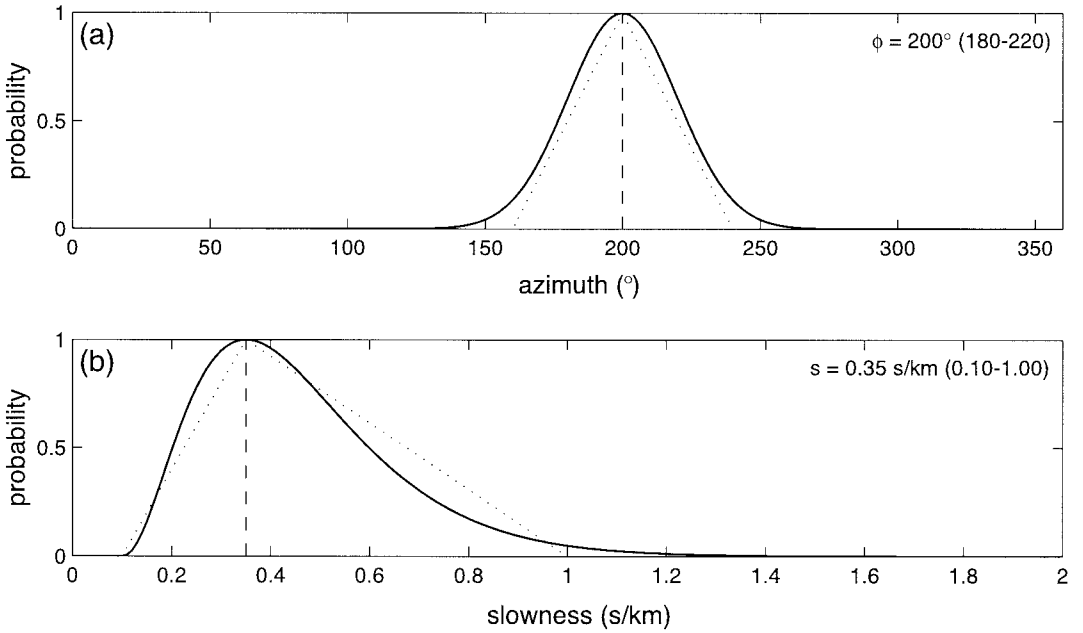

Figure 2. Probability distributions used in the source location procedure. (a) Gaussian distribution (solid line) for azimuth, centered on the mean value (200°), with a standard deviation equal to a half of the difference between the error limits. (b) Poissonian distribution (solid line) used for slowness. The maximum corresponds to the average value and reaches 0 at the lower error limit and 5% of the maximum at the higher error limit. Dotted curves are triangular probability distributions used to test the effect of our choice of the Gaussian and Poissonian functions on the source locations.

stations that compose the seismic antenna, but we do not consider such a small effect. For slowness, the value of zero is a cutoff, and it makes no sense to define a probability distribution that includes negative values. Therefore the probability distribution for slowness must be asymmetric. On the basis of these a priori considerations, we select a Gaussian distribution for the azimuth and a Poissonian distribution for the apparent slowness. Both distributions are well-known, commonly used functions. The particular definitions are

$$P_\phi^A(x, y, z) = \exp\left[-2\left(\frac{\phi^A(x, y, z) - \bar{\phi}_0^A}{\bar{\phi}_{\max}^A - \bar{\phi}_{\min}^A} \right)^2 \right], \tag{11}$$

$$P_s^A(x, y, z) = \left(\frac{s^A(x, y, z) - \bar{s}_{\min}^A}{\bar{s}_0^A - \bar{s}_{\min}^A} \right)^{\kappa^A} \cdot \exp\left(- \frac{s^A(x, y, z) - \bar{s}_0^A}{\bar{s}_0^A - \bar{s}_{\min}^A} \kappa^A \right) \qquad s^A > \bar{s}_{\min}^A, \tag{12a}$$

$$P_s^A(x, y, z) = 0 \qquad s^A \le \bar{s}_{\min}^A, \tag{12b}$$

where

$$\kappa^A = \log 0.05 \left(\log \frac{\bar{s}_{\max}^A - \bar{s}_{\min}^A}{\bar{s}_0^A - \bar{s}_{\min}^A} - \frac{\bar{s}_{\max}^A - \bar{s}_0^A}{\bar{s}_0^A - \bar{s}_{\min}^A} \right)^{-1}, \tag{13}$$

$$(x, y, z) \in \text{domain}, \qquad A \in \text{arrays}.$$

In our application these probability functions are defined in such a way that their maximum value (which is 1) corresponds to the average value of the parameters obtained from experimental analysis of a seismic event and the width of the distribution is defined by the error limits in the experimental parameters. The shape of these functions is shown by the solid lines in Figure 2. For the Gaussian function we select a standard deviation equal to a half of the average azimuthal error in the first-arrival window. For the Poissonian function we use the extremes of slowness (i.e., the minimum and maximum, including the error limits) instead of the averages to define the shape of the curve. The probability is zero for values below $\bar{s}_{\min}^A$ and 5% of the maximum at $\bar{s}_{\max}^A$.

The functions $\phi^A(x, y, z)$ and $s^A(x, y, z)$ in (11) and (12) represent the azimuth and apparent slowness of the waves defined at each array as a function of the source coordinates. These functions constitute what we call the slowness vector model, which allows us to successfully apply the location method. The slowness vector model is basically a vector field, which assigns to every point in the investigated domain the corresponding apparent slowness vector as it ought to be measured at array A for a given model of the medium. The slowness vector model depends, of course, on the structural model selected to represent the medium and on the position of the antenna. In sections 4 and 5 we address the problem of finding a slowness model adequate for the problem of locating the source of LP seismicity at Kilauea Volcano, Hawaii.

4. Simple Slowness Models

The simplest slowness vector model is that obtained for a homogeneous half-space, in which the slowness vector is directly related to the source-array geometry. Once the velocity of the medium is fixed, the apparent slowness depends only on the incidence angle because the ray paths are straight lines. Wave fronts propagating across the array always move radially outward from the source, and the back azimuth points to the epicenter. The azimuth and slowness for waves propagating from a source located at (x, y, z) within an homogeneous medium are

$$\phi^A(x, y, z) \equiv \phi^A(x, y) = \pi + \arctan\frac{x - x_A}{y - y_A} \tag{14a}$$

$$s^A(x, y, z) = \left(v\sqrt{1 + \frac{(z - z_A)^2}{(x - x_A)^2 + (y - y_A)^2}} \right)^{-1}, \tag{14b}$$

where (x_A, y_A, z_A) represent the coordinates of the center of the array and v is the velocity of the medium.

Further model complexity may be introduced by considering a horizontally stratified medium. The underlying geometric idea still applies, but now the ray paths are no longer straight lines. Rather they are segmented lines contained in a vertical plane, with no lateral deviations. Thus the relation for azimuth remains exactly the same. The corresponding relation for slowness is slightly more complex because we have to introduce the thicknesses and velocities of the different layers, and the resulting equation needs to be solved numerically. For example, for a layered medium with velocities v_n and layer thicknesses h_n, the relationship between the apparent slowness of the direct arrival (equivalent to the ray parameter) and the source depth for a source located in layer N is given by [*Chouet*, 1996b]

$$z_A - z = \sum_{n=1}^{N-1} h_n + \frac{\sqrt{1 - (s^A(x, y, z)v_N)^2}}{s^A(x, y, z)v_N} \cdot \left(\sqrt{(x - x_A)^2 + (y - y_A)^2} - \sum_{n=1}^{N-1} \frac{h_n s^A(x, y, z)v_n}{\sqrt{1 - (s^A(x, y, z)v_n)^2}} \right). \tag{15}$$

We refer to the above models as geometric slowness vector models. In this paper, we use these models in a restricted way to obtain preliminary information about the source epicenter. Basically, we assume that there is no a priori knowledge of the variation of apparent slowness with the source coordinates, so that the source depth cannot be determined. We use $P_s^A(x, y, z) = 1$ as a representation of this lack of information and are satisfied with a determination of the epicentral region using only azimuthal information. In the general case, however, when the effects of topography and lateral heterogeneities are not expected to be strong, full advantage may be taken of this method by including the information from both azimuth and slowness.

5. Synthetic Slowness Model for Kilauea Volcano

Volcanoes typically have complex velocity structures and sharp topography, both of which distort the wave fields in a way that is not easy to guess a priori. Therefore the above slowness vector models based on laterally homogeneous half-spaces are too simple to be realistic in applications to waves with frequencies in the 1–10 Hz range. As an illustration of how we can generate more complex models that include the effects of topography and three-dimensional (3-D) velocity structure, we now consider a model appropriate for the Kilauea summit region, where we have accurate information about topography and good quality knowledge of the 3-D velocity structure [*Okubo et al*., 1997; *Dawson et al*., 1999]. We use this information to account for the effects of lateral heterogeneities and to obtain a more reliable solution for the source location.

The procedure for obtaining a slowness vector model relies on the generation of synthetic seismograms intended to reproduce as closely as possible the behavior of the observed wave field by including the effects of topography and 3-D velocity structure. This procedure consists in a discretization of the medium using a uniformly spaced 3-D grid and computation of the free surface response at each antenna produced by seismic sources located at each node of the gridded domain. Frequency-slowness analyses in the synthetic data yield estimates of slowness and azimuth for each source. The ensemble of slowness and azimuth estimates calculated for all the sources constitutes the slowness vector model. This model can then be compared to the observed slowness vector data to obtain a maximum likelihood solution for the source position.

5.1. Synthetic Seismograms

We generate the synthetic seismograms by the finite difference method of *Ohminato and Chouet* [1997], in which we include information about the topography and the three-dimensional velocity structure of Kilauea.

The domain used for the computation of the wave field is centered at a point located near the eastern edge of the Halemaumau pit crater, at approximately 19°24.5′N, 155°17.0′W (Figure 3). The domain size is $10 \times 10 \times 4$ km, and the cell size is $40 \times 40 \times 40$ m, yielding a 3-D mesh with $251 \times 251 \times 101$ nodes. The maximum elevation is 1408 m at the northwest corner of the domain. We use this elevation as the top elevation of the computational domain. We take the elevation of 1088 m as the zero depth level, with depth defined as positive downward. The 1088-m elevation represents the average elevation of the caldera floor. The size of the selected domain is small enough to keep computation times within a reasonable range but large enough to minimize the amplitudes of any spurious reflections from the sides and bottom.

The topography of Kilauea is obtained from the U.S. Geological Survey (USGS) digital elevation map (DEM) of the island of Hawaii. Although the resolution of the DEM is 10 m, we resample these data at 40 m to make them compatible with our computational mesh.

The P and S wave velocity structures are those derived by *Dawson et al*. [1999], corrected for an error in their initial S wave velocity model. They used a data set comprising 206 earthquakes recorded at 67 stations to obtain a 3-D P and S wave velocity model of the Kilauea summit region with a resolution of 500 m. Their results show the presence of a 10–20% low-P wave velocity anomaly extending beneath Halemaumau and the southern and southwestern part of the caldera. We perform a 3-D interpolation of the 500-m data to match the grid spacing of 40 m in our model and use the topography to define as empty (Lamé coefficients equal to 0) all the cells above the free surface.

The last step in fixing the properties of the domain is to introduce the density. Unfortunately, no accurate information is available on the density of rocks within Kilauea caldera. Therefore we use the empirical relation between compressional wave velocity and density determined by *Nafe and Drake* [1963]. For the range of compressional wave velocities between 3 and 7 km/s, this relation can be approximated by the linear function

$$\rho = 1740 + 160v_p, \tag{16}$$

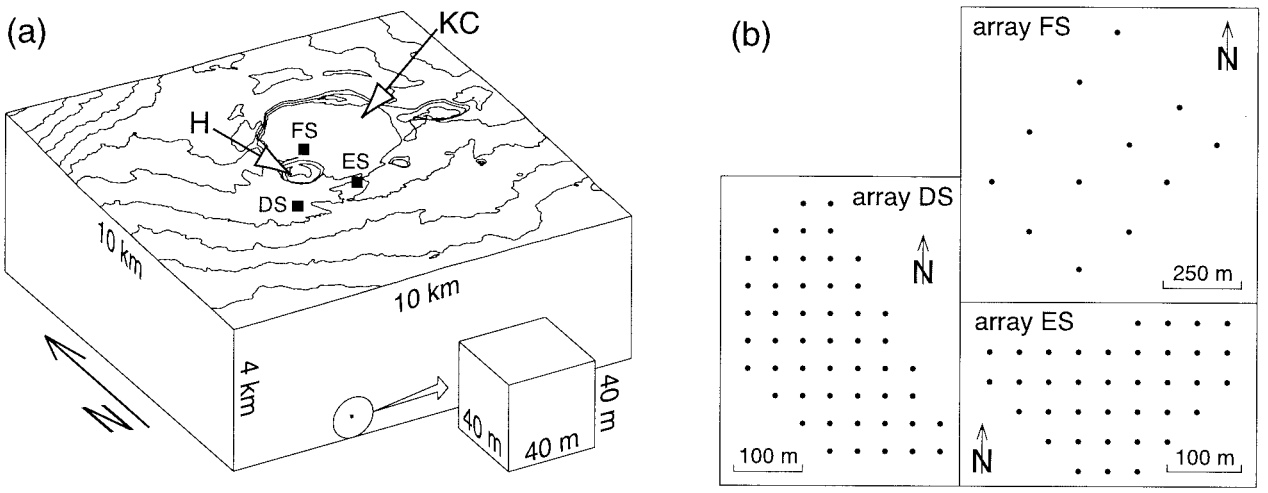

Figure 3. (a) Domain selected for the finite difference calculations. The sketch shows the domain dimensions, grid size, and location of the centers of the synthetic arrays (solid squares FS, ES, and DS). KC identifies Kilauea caldera and H indicates the Halemaumau pit crater. (b) Configurations of the synthetic arrays.

in which the density ρ is expressed in kg/m^3 and the compressional velocity v_p is in km/s.

In the present analysis the source time function and source mechanism are not important as we are only interested in the directional properties and propagation velocities of the waves composing the wave field. We select a source time function in the form of a cosine with period of 0.5 s, which is appropriate for the grid spacing of 40 m and velocities of the medium as determined by *Dawson et al.* [1999]. We consider an isotropic point source with dipole moment of 10^{12} N m. The time step for the finite differences is set to 3 ms to satisfy the Courant stability criterion [*Ohminato and Chouet*, 1997].

5.2. Description of the Synthetic Wave Field

We calculate two different sets of synthetics in order to understand separately the effects of topography and structure on the features of the wave field generated by a point source. Our first model consists of a homogeneous medium with *P* and *S* wave velocities of 4 and 2 km/s, respectively, and includes only topography. The second model includes both topography and the *P* and *S* wave velocity structures as determined by *Dawson et al.* [1999].

Plate 1 shows snapshots of the vertical component of displacement at the free surface generated by an isotropic point source embedded in a homogeneous medium with topography. The source is located at a depth of 520 m beneath the northeast edge of Halemaumau. The composition of the wave field is dominated by waves propagating radially outward from the source, but many other effects are apparent. Diffraction of the incident *P* wave by Halemaumau is observed as a distinct red patch on the floor of this pit crater at 0.5 s. Wave diffraction by Halemaumau is also apparent in the snapshot at 0.9 s, where it manifests as a notch of lighter blue in the dark blue ring marking the second peak of the wave front near the southwest edge of the pit crater. The bright triangular orange patch observed near the source epicenter in this snapshot identifies converted *SV* waves reflected from the edge of Halemaumau facing the source. Waves are generated at the circular bottom corner of Halemaumau by the incident *P* wave. These waves travel along the floor of the pit crater where they interfere constructively to create a pattern of standing circular waves. These trapped waves are observed as a bright patch of orange near the center of Halemaumau at 0.9 s and appear as a bright orange ring coincident with the walls of Halemaumau at 1.2 s. Rayleigh waves scattered by the pit crater are observed as orange-colored rings propagating outward from Halemaumau at 1.5 s and 2.1 s. Wave diffraction by a smaller pit crater east-southeast of Halemaumau and by cliffs flanking the caldera to the north are observed in the snapshot at 0.9 s where they appear as orange-colored notches embedded in the dark red ring identifying the trough in the *P* wave front. Waves backscattered from cliffs marking the northwest caldera boundary appear as a linear band of orange oriented parallel to the topography contours north of Halemaumau at $t = 1.2$ s. These waves propagate in a clockwise direction through the northern sector of the caldera where they interfere with the Rayleigh waves scattered by Halemaumau to produce a wave pattern identified by the orange patches located near the northern caldera boundary at 1.5 s and 2.1 s. Waves backscattered by cliffs flanking the northern sector of the caldera are also observed propagating southward past the southern edge of Halemaumau at 3.3 s. The mottled pattern of yellow on the caldera floor observed in this snapshot represents decaying standing waves resulting from the interference of waves backscattered by the topography of the caldera.

The main features of the wave field associated with the topography of Kilauea remain essentially unchanged when the three-dimensional *P* and *S* wave velocity structures of the medium are taken into account. Plate 2 shows a snapshot of the free surface vertical displacement wavefield calculated for a medium including both topography and velocity structure. The source is located at a depth of 200 m beneath the northeast edge of Halemaumau. The effect of the velocity structure is a distortion of the features observed in the presence of topography only, caused by the different velocities in different parts of the domain.

The apparent slowness and propagation azimuth of the waves are different in the model including topography only, compared to the model that includes both topography and structure. The arrows in Plate 2 represent the slowness vectors

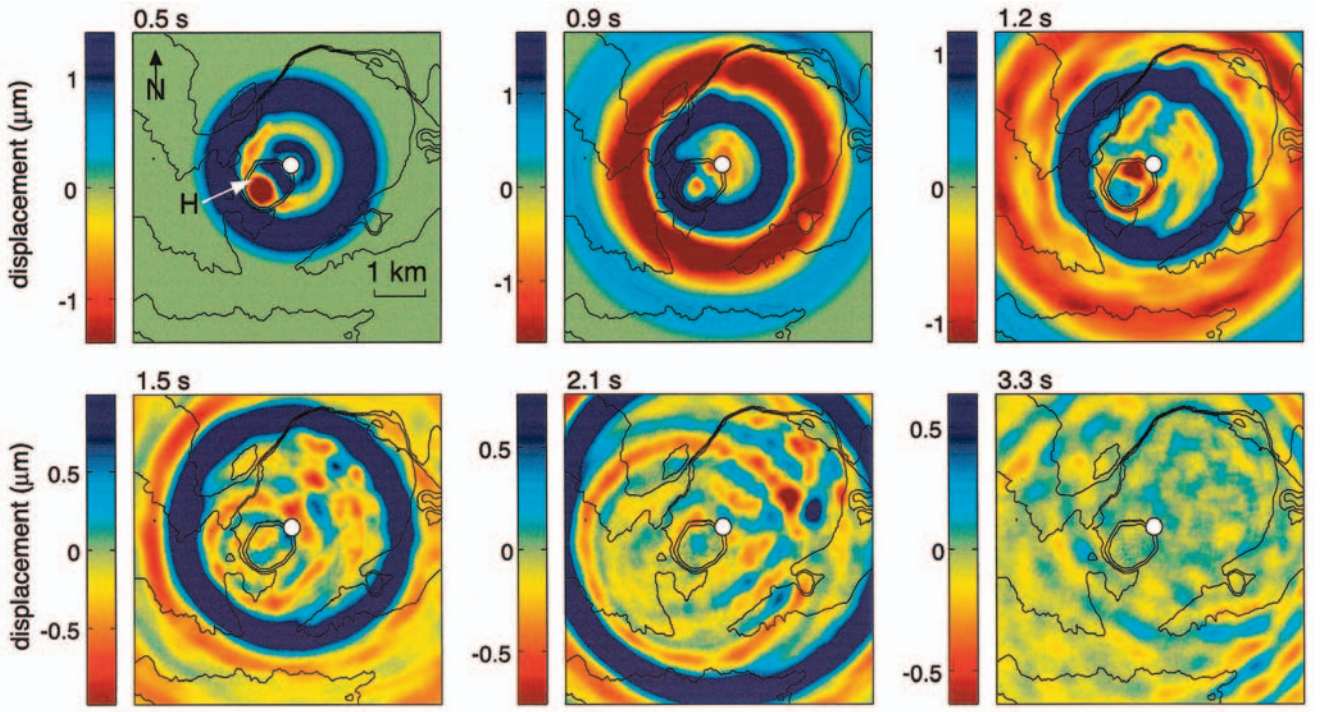

Plate 1. Snapshots of the vertical component of the free surface displacement wave field produced by a point source with epicenter marked by the white circle. H indicates the Halemaumau pit crater. The medium is homogeneous and includes topography. The time elapsed from the origin time of the synthetic event is shown at the top of each panel.

determined at the three synthetic antennas shown in Figure 3 (the procedure used to obtain these estimates is explained in section 5.3). The differences between the slowness vectors derived from the two models are quite large and indicate that a homogeneous medium, even if it includes the effect of topography, is not a good enough representation of the Kilauea summit region, at least for the purpose of defining a slowness vector model.

5.3. Frequency-Slowness Analyses of Synthetic Events

To obtain estimates of the slowness vector as a function of source position, we need to apply the frequency-slowness method to the synthetic data. To do so, we generate synthetic seismograms at 100 stations distributed in three arrays named DS, ES, and FS in Figure 3. The locations and configurations of these arrays are selected to simulate the setups of three antennas deployed at Kilauea in February 1997 [*Almendros et al.*, this issue]. We select a sampling interval of 15 ms and synthetic seismogram length of 3.75 s, adequate choices for the purpose of determining the apparent slowness and azimuth of the first arrival at each antenna. The frequency-slowness analyses are performed with a sliding window length of 1.92 s (128 samples) and overlap of 0.2 s. Because of the limited bandwidth of the synthetic source, we use only one frequency band with a bandwidth of 2.6 Hz centered at 2 Hz, and we do not perform slowness stacking. In this way, we obtain a slowness vector at each of the arrays for a given source position. By defining a grid of source positions, we obtain a 3-D slowness vector model for each antenna.

Because of the larger aperture of array FS, the wave fronts propagating through the antenna are not perfectly approximated by a plane wave front for a source located close to this

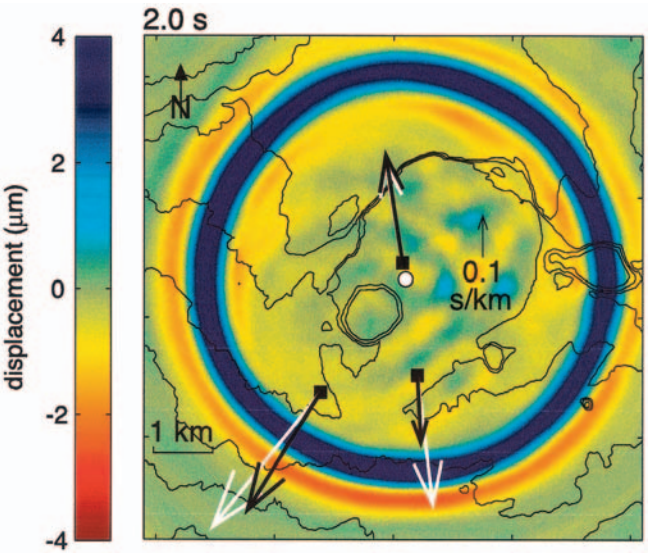

Plate 2. Snapshot of the vertical component of the free surface displacement wave field 2.0 s after the origin time of a synthetic event. The medium includes both the topography and 3-D velocity structure of Kilauea. The epicenter of the point source is identified by the white circle. The arrows represent the slowness vectors estimated at three arrays (see Figure 3) for a homogeneous medium including topography (white arrows) and a medium including both topography and structure (black arrows). Differences are relatively large and affect both the azimuth and apparent slowness. These results emphasize the importance of considering both topography and structure in the definition of a synthetic slowness vector model.

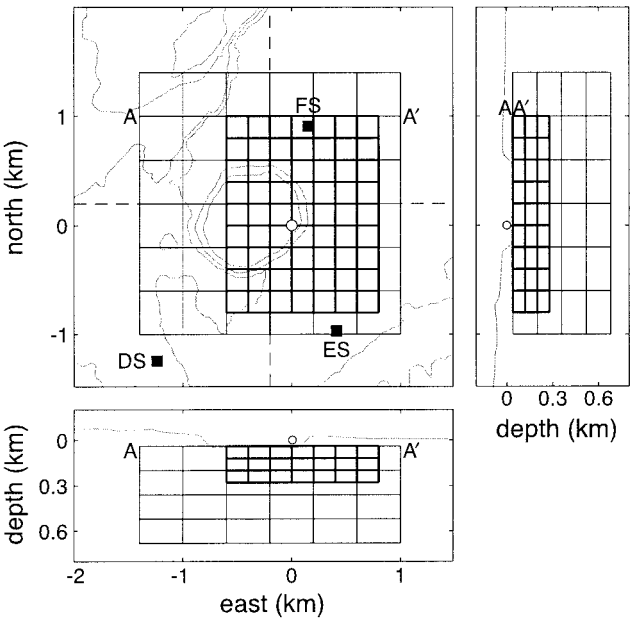

Figure 4. Map view and east-west and north-south vertical cross sections of the source domain selected for the generation of a synthetic slowness vector model. The positions of the cross sections are indicated by the dashed lines in the map view. The selected domain is bounded by the larger 2.40 × 2.40 × 0.64 km gridded region. Light lines define a coarser 400 × 400 × 160 m grid, and bold lines define a finer 200 × 200 × 80 m grid. The origin of the model coordinates is shown by the open circle. The positions of the antennas are marked by solid squares. A-A′ is the profile used in our selection of the appropriate source grid spacing (see Figure 5).

array. The MUSIC method does provide a best fit plane wave solution for the azimuth and slowness, but the power is usually lower, pointing to a lack of coherence due to the large distance between stations (200 m). A circular wave front approximation [*Almendros et al*., 1999] might be more appropriate in this case. Unfortunately, the high apparent velocities of the direct waves in the model, even for shallow sources, make this approach difficult to apply. However, being close to the source is also convenient, because the ray paths are short and the waves are not significantly perturbed by the scattering due to topography and shallow velocity heterogeneities, as demonstrated by the coincidence of the black and white arrows at array FS in Plate 2.

5.4. Synthetic Slowness Vector Model

The first step in establishing a synthetic slowness vector model is to define the region of interest. On the basis of preliminary locations of LP seismicity recorded in the summit caldera [*Almendros et al*., this issue], we know that most of the seismic activity we are interested in is located in an area near the eastern edge of Halemaumau. Accordingly, we develop a slowness vector model for a region of 2.40 × 2.40 × 0.64 km centered on Halemaumau (Figure 4).

The second step is to define an appropriate source grid spacing. Figure 5 shows the components of the slowness vector calculated at each of the three antennas for sources distributed along profile A-A′ in Figure 4. The plots show the slownesses and the azimuthal deviations from the source-receiver directions, calculated for sources distributed every 40 m (dotted line), 200 m (solid line), and 400 m (dashed line) along the profile. Many sharp oscillations are observed in the parameters determined with a source spacing of 40 m. These oscillations mainly reflect the effects of topography. This conclusion is supported by our observation that the oscillations become smoother with increasing source depths. The velocity structure we are using is very smooth, as it represents an interpolation from a model with spatial resolution of 500 m and therefore cannot by itself explain the irregular spatial pattern of the slowness vector.

The natural tendency to make the grid spacing as small as possible, down to the 40 m grid used in the finite difference calculation of synthetic seismograms, is not the best idea for two reasons: (1) the process of computing the free surface motion for a single synthetic source, as described above, is time consuming (about 7 hours in a 450 MHz computer) and (2) the velocity structure is only known with a resolution of 500 m, so that it makes no sense to compute synthetics to such a level of detail. We select a grid spacing of 200 m, small enough to adequately reproduce the spatial variation of slowness but large enough to make the computation of a relatively large source domain feasible.

The synthetic sources are positioned at individual grid nodes in a uniformly spaced grid extending from −0.6 to 0.8 km in the east-west direction, from −0.8 to 1.0 km in the north-south direction, and from 40 to 280 m in the depth direction. We use source grid spacings of 200 m in the north-south and east-west directions and 80 m in the depth direction. The total number of point sources considered is 304. Because of the topography of Halemaumau, sources in the top layer of the model within the walls of the pit crater are located above the topography and thus are not considered in our calculations. Slowness vectors corresponding to these sources are estimated afterward by interpolation. This artifact is used in order to provide a uniform grid, even with the a priori knowledge that no source is located above the topography. Once our treatment of the data has been completed, we reject the information from every point above the floor of Halemaumau.

For completeness, we also compute slowness vectors for another set of sources extending from −1.4 to 1.0 km in the east-west direction, from −1.0 to 1.4 km in the north-south direction, and from 40 to 680 m in the depth direction. The grid spacings used for this set of sources are 400 m in the north-south and east-west directions and 160 m in the depth direction. In this way, an additional 205 noncoincident sources are added to the model, yielding a total of 509 point sources. The use of a coarser 400-m grid spacing is justified for deeper sources because the spatial variations of the slowness vector are not as sharp for such sources. It should be noted that the preliminary source locations for most of the actual seismic sources considered in our study [see *Almendros et al*., this issue] fall within the limits of the 200-m grid, so that an extension of the 200-m grid to the boundaries of the larger domain is not warranted. The final model relating the slowness vector with the source position for each array, which we call the synthetic slowness vector model, is produced by merging the results from both grids and interpolating to a grid spacing of 40 m in the horizontal directions and 20 m in the vertical direction.

Figure 6 shows the resulting slowness vector models obtained for each synthetic antenna, decimated to a 400-m spacing. The arrows represent the slowness vectors measured at the synthetic antennas. The tail of each individual arrow is positioned at the source location. This picture is the equivalent of

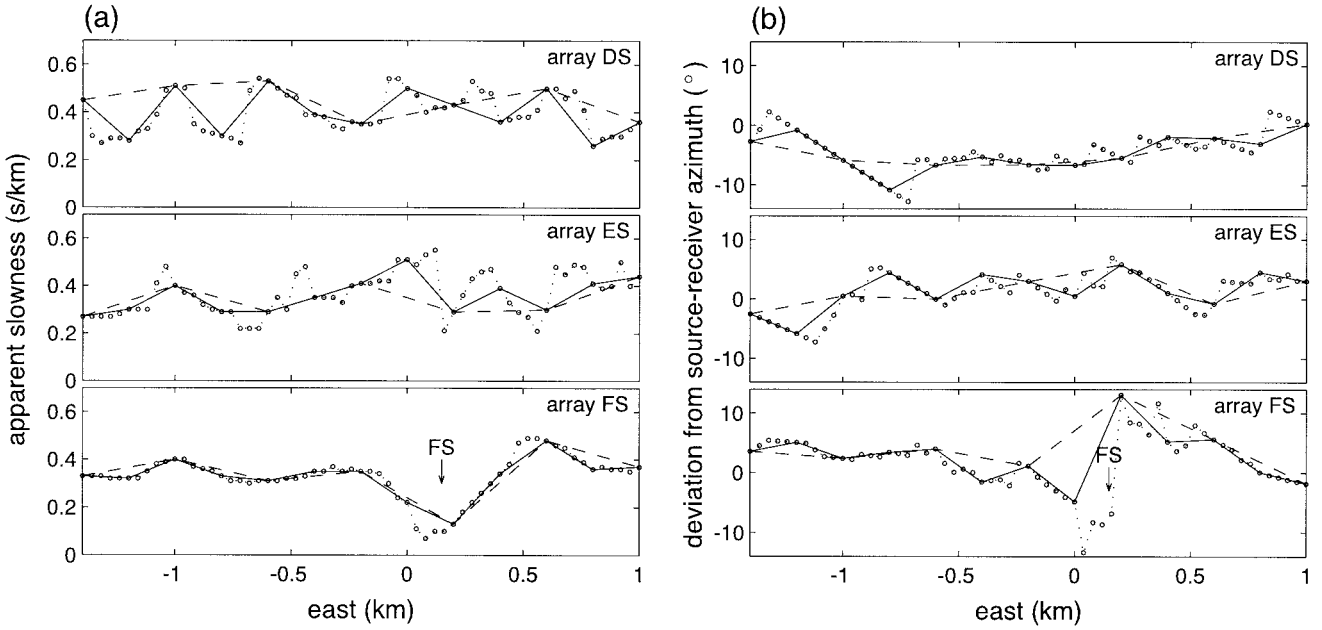

Figure 5. (a) Apparent slowness and (b) azimuthal deviation from the source-receiver direction, calculated at antennas DS, ES, and FS, from top to bottom, respectively, for synthetic sources distributed along east-west profile A-A′ in Figure 4. This profile extends from −1.4 to 1.0 km in the east-west direction and is located 1.0 km north of the origin, at a model depth of 40 m. The arrows in Figures 5a (bottom) and 5b (bottom) mark the position of array FS, which is very close to the profile. The apparent slowness at this antenna is very small for nearby sources, and thus the errors in azimuth are correspondingly larger. The dashed, solid, and dotted lines represent source grid spacings of 400, 200, and 40 m, respectively. The 200-m grid is our selected trade-off choice to represent the source domain because it adequately reproduces the basic behavior of the parameters and keeps the model computation time within reasonable limits.

(14) and (15) for a model that includes topography and 3-D velocity structure.

6. Example: Location of a Synthetic Event

We use a synthetic event, generated in the same way as described in section 5, to discuss the location capabilities of our method. The source coordinates in the east, north, and depth directions are 200, 400, and 120 m, respectively (see Figure 4).

Figure 7 illustrates the first step in our location procedure, which is a frequency-slowness analysis of the synthetic wave field. Figures 9a, 9b, and 9c show the results obtained with the DS, ES, and FS antennas, respectively. Figure 9d shows the average values of azimuth and slowness, as well as the error ranges, within the first-arrival windows identified by the shaded bands in Figures 9a–9c. The white circle in the map view marks the original epicenter location, which is positioned within the overlap of the azimuthal error wedges.

In the next step, we use the restricted geometric model to determine the epicenter location for this synthetic event. The 2-D azimuthal probability distributions involved, obtained by application of (11) and (14), are shown in Plate 3 together with the combined source location probability, which is the product of the three azimuthal probability distributions (equation (9)). The maximum probability, which we assume to be the epicenter location, occurs at coordinates (200, 560) m. The size of the 80% error region is about 240 × 800 m, and the location quality is 0.9. The distance between this solution and the actual epicenter, marked by the white circle in Plate 3, is 160 m. Location errors of this magnitude are very common when using the geometric model. These errors generally increase with distance from the antennas, but even within the region between the antennas they may range up to 500 m. The reason is that this model does not account for deviations in the wave fronts caused by topography and lateral velocity heterogeneities. These effects, which are included in the calculation of the synthetic seismograms, can lead to azimuthal deviations of up to 10°.

If we use the synthetic model instead, we can go one step further and obtain an estimate of the source depth along with a better constraint on the epicenter location. The steps followed in the location procedure are illustrated in Plate 4. The map views are of the shallowest layer and north-south vertical cross sections through the 3-D probability distributions. Plates 4a–4c show the spatial probability distributions for azimuth obtained at each antenna. Dashed white lines mark the average geometric back azimuths and provide a measure of the bias due to the effects of topography and structure. Plates 4d–4f show the spatial probability distributions for slowness obtained at each antenna. These distributions are obtained from an application of (11) and (12) to the slowness vector model depicted in Figure 6. Plates 4g, 4h, and 4i represent the combined azimuthal probability, combined slowness probability, and total probability distribution including azimuth and slowness, respectively, and represent the spatial source probability as defined in (9). In this example, the maximum probability coincides with the source position (white circle) at coordinates (200, 400, 120) m. The size of the error region, marked by the solid black line, is 160 × 320 × 160 m, and the location quality is 1.0.

Plate 5 shows other examples, equivalent to Plate 4i, for

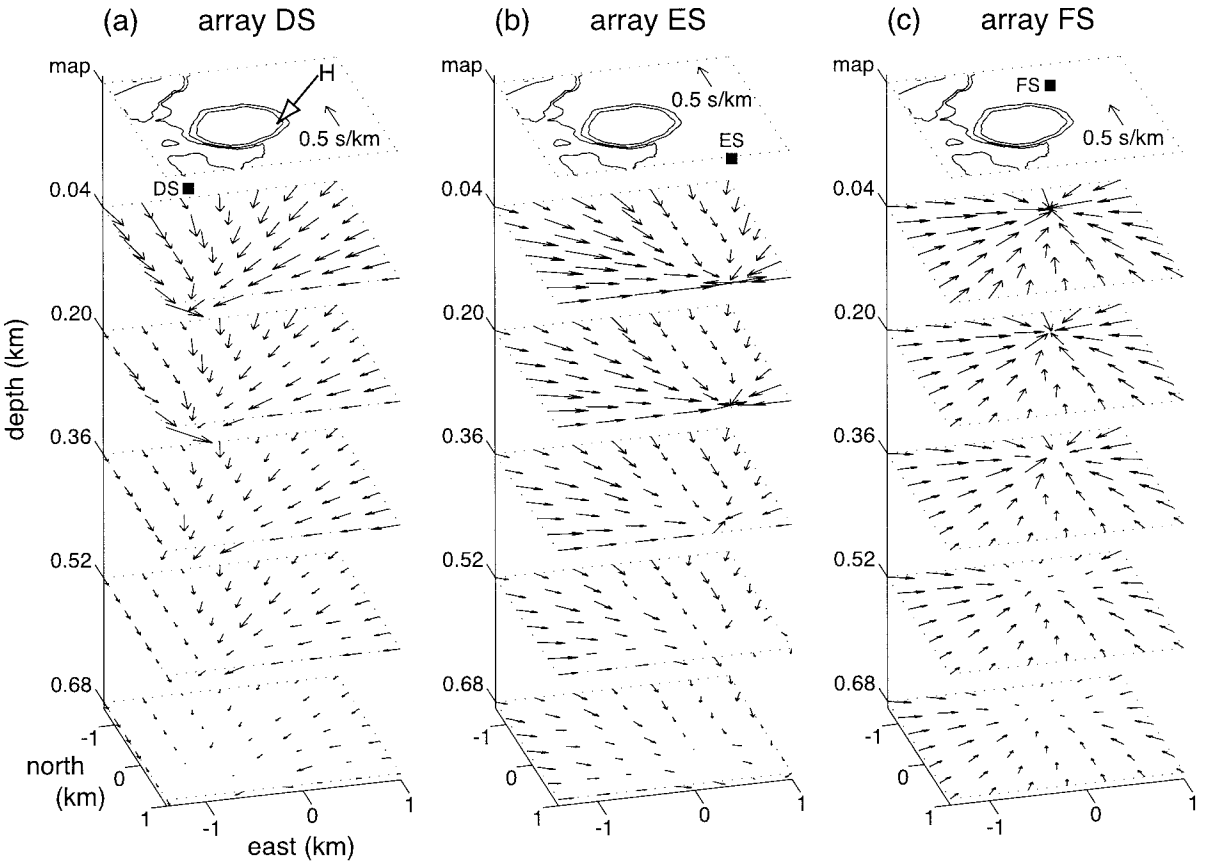

Figure 6. Three-dimensional views of the decimated synthetic slowness vector models obtained for the (a) DS, (b) ES, and (c) FS antennas. Each arrow represents the slowness vector measured at the corresponding antenna for a synthetic point source located at the beginning of the arrow. The magnitude of the arrow represents the slowness value according to the scale shown. At the top of each model is a contour map, which shows the position of the antenna (solid square). H indicates Halemaumau.

sources located at other positions in the domain. The picture of the obtained source is blurred by limitations in the resolving capabilities of the antennas and by the complexities of the structure. Even for a simple point source, the spatial source probability determined by our procedure is not a point-like region but is an extended distribution. The low-probability tails present in the solutions (i.e., the blue-to-yellow regions in Plate 5) are artifacts of the method caused by the array configurations and model limitations. The colored patterns in Plate 5 may be intuitively interpreted as the impulse response of our model. Ideally, it would be desirable to deconvolve this response and to obtain a delta-like location. However, to proceed with such deconvolution, we would need to calculate a spatial source probability for sources located at every node in the domain, an onerous procedure that is not justified in light of our simplistic model. The tails are more pronounced in the region immediately east of Halemaumau and are usually elongated in the north-south direction. In spite of these limitations, there is no ambiguity in the source location because the absolute maximum is generally well defined and matches the already known source locations. Secondary peaks in the spatial source probability distributions, if any, amount to only a fraction of the dominant peak.

7. Capabilities of the Method

For the remainder of this discussion we focus on the use of the synthetic model and address a few important questions concerning its capabilities. First, how precise is the method? We want to know if it gives back the correct source position, within the error limits, when the source position is known. Second, how sensitive is the method to errors in the data? Does the method provide a different result for data with very similar parameters, or is it stable? Last, how sensitive is the solution to the functions used to represent the probability distributions?

7.1. Accuracy and Resolution

To investigate the accuracy and resolution of our method, we relocate a subset of synthetic sources used to calculate the slowness vector model. The selected sources are located at the nodes of the 400-m grid domain. We know the source position and also the corresponding values of azimuth and slowness at each antenna. From the perspective of the model these azimuthal and slowness values represent true values. For most of the sources the maximum of the source location probability matches the actual source position with a location quality close

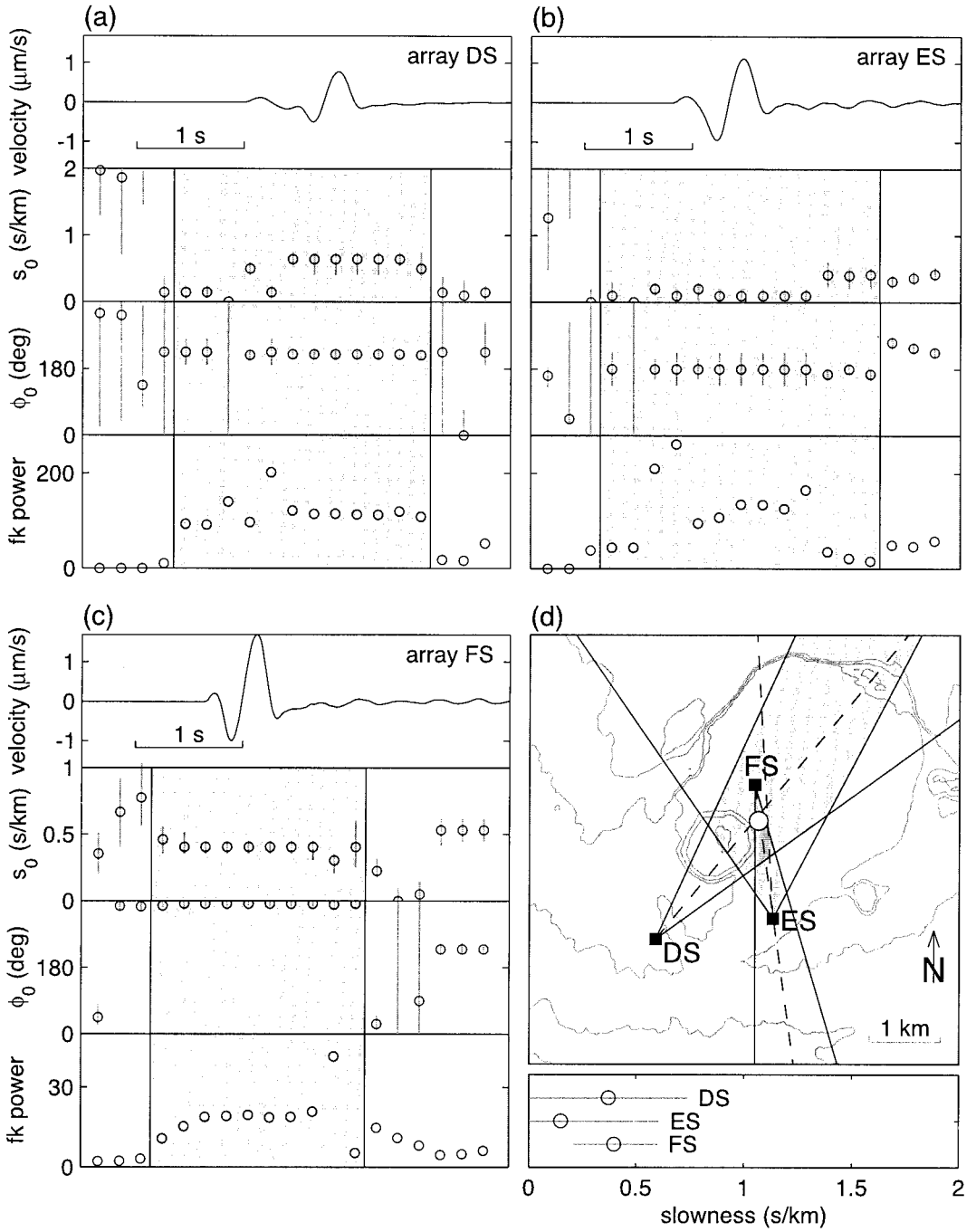

Figure 7. Examples of results obtained from frequency-slowness analyses of the wave field produced by an isotropic point source with a 2-Hz cosine source-time function. From top to bottom, the seismogram generated at a selected array site, the apparent slowness, azimuth, and peak slowness power determined at the array are shown. (a) Results obtained at array DS, (b) results for array ES, and (c) results for array FS. The bands of shading identify the first-arrival windows (see text for explanations). (d) Graphic summary of the frequency-slowness results. (top) Map showing a tentative epicentral region defined by the overlap of the shaded wedges. These wedges represent the back azimuthal spread resolved by each array, with the dashed lines indicating the average back azimuth determined over the first-arrival window. The white circle marks the epicenter of the synthetic event. (bottom) Average slowness in the first-arrival window determined at each antenna.

to 1. A mislocation amounting to a few nodes is only observed for sources located deep below one of the antennas. This indicates that the performance of our method is homogeneous within the entire domain; that is, there is no tendency of the method to preferentially assign the source to any particular region in the domain.

However, the estimate of the slowness vector obtained from the frequency-slowness analysis of a synthetic event is not

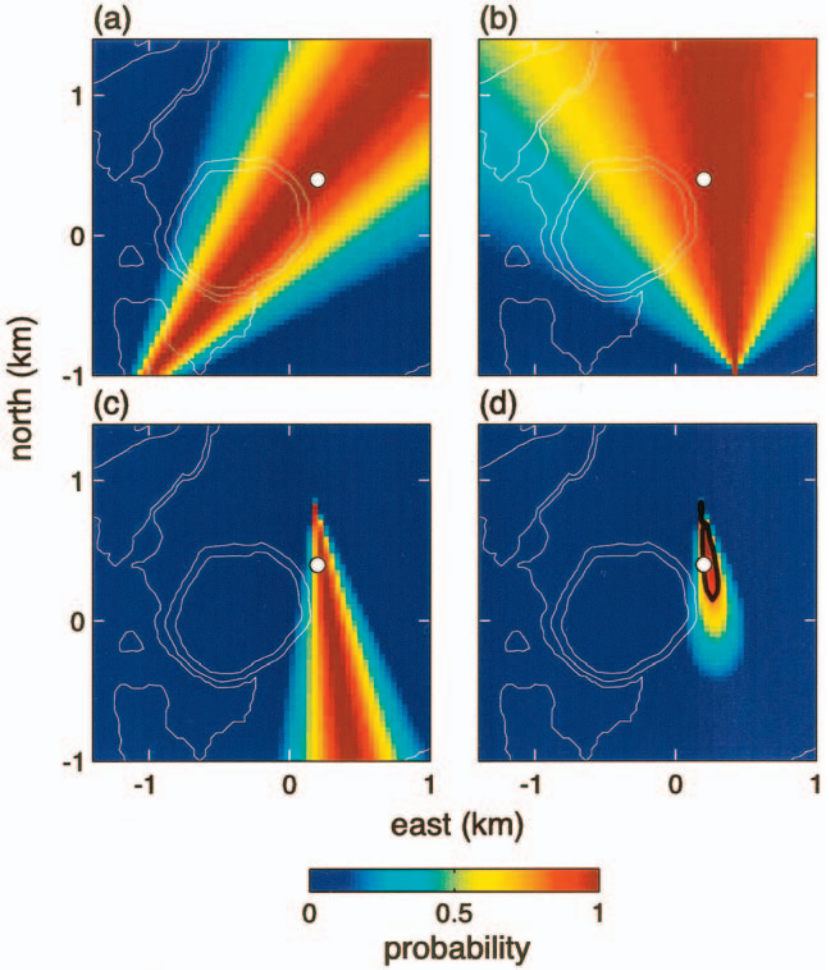

Plate 3. Azimuthal probability distributions for the location of a synthetic event determined from the restricted geometric model. The white circle marks the source epicenter. (a) Azimuthal source location probability obtained from the DS antenna. (b) Azimuthal probability derived from the ES antenna. (c) Azimuthal probability from the FS antenna. (d) Combined source location probability showing the epicentral location and the error boundary defined by the 80% probability contour (bold black line).

always well reproduced by our model. When the source location does not coincide with one of the nodes of the source grid shown in Figure 4, the model cannot reproduce exactly the value of azimuth and especially that of slowness. To illustrate this model limitation, let us consider again the azimuth and slowness profiles in Figure 5 and compare the values obtained from frequency-slowness analysis of the synthetic events (open circles) with the values obtained by interpolation over the 200-m grid model (solid line). The differences in estimated values may amount up to around 0.1 s/km in slowness and 10° in azimuth, but the effects of such differences are usually minimized by the fact that these discrepancies do not simultaneously affect all six parameters of the method. The locations obtained for several test sources located between grid nodes have smaller location quality and are usually misplaced by several nodes, especially in the shallowest (40 m deep) layer. The mislocation errors may range up to 200 m. The reason for these errors is the high variability of the slowness vector over short distances (see Figure 5). Such rapid variations in slowness are beyond the resolution of our slowness vector model. The errors decrease with depth, reflecting the decrease in the amplitude of slowness fluctuations associated with deeper sources. To achieve higher resolution, we would need to calculate a slowness vector model for point sources distributed over a finer grid. However, taking into account other factors such as the resolution of the antennas and spatial resolution of the velocity structure, we consider the present model to be adequate, keeping in mind that the locations are estimated with errors on the order of 200 m. This error radius is roughly equivalent to the size of the 80% probability isosurfaces. Therefore we may consider that the region within the 80% isosurface is a good estimate of the uncertainty of the source position.

7.2. Stability

There are several effects that could induce errors in the estimates of the slowness vector of the wave field, for example, the presence of near-surface inhomogeneities beneath the individual instruments composing the antenna, which would distort the arriving wave fronts, or the analysis of signals with a low signal-to-noise ratio. To test the stability of the method and assess its sensitivity to errors in the data, we introduce random variations in the average values of azimuth and slowness derived from frequency-slowness analyses prior to applying the location method, and we compare the relocated source

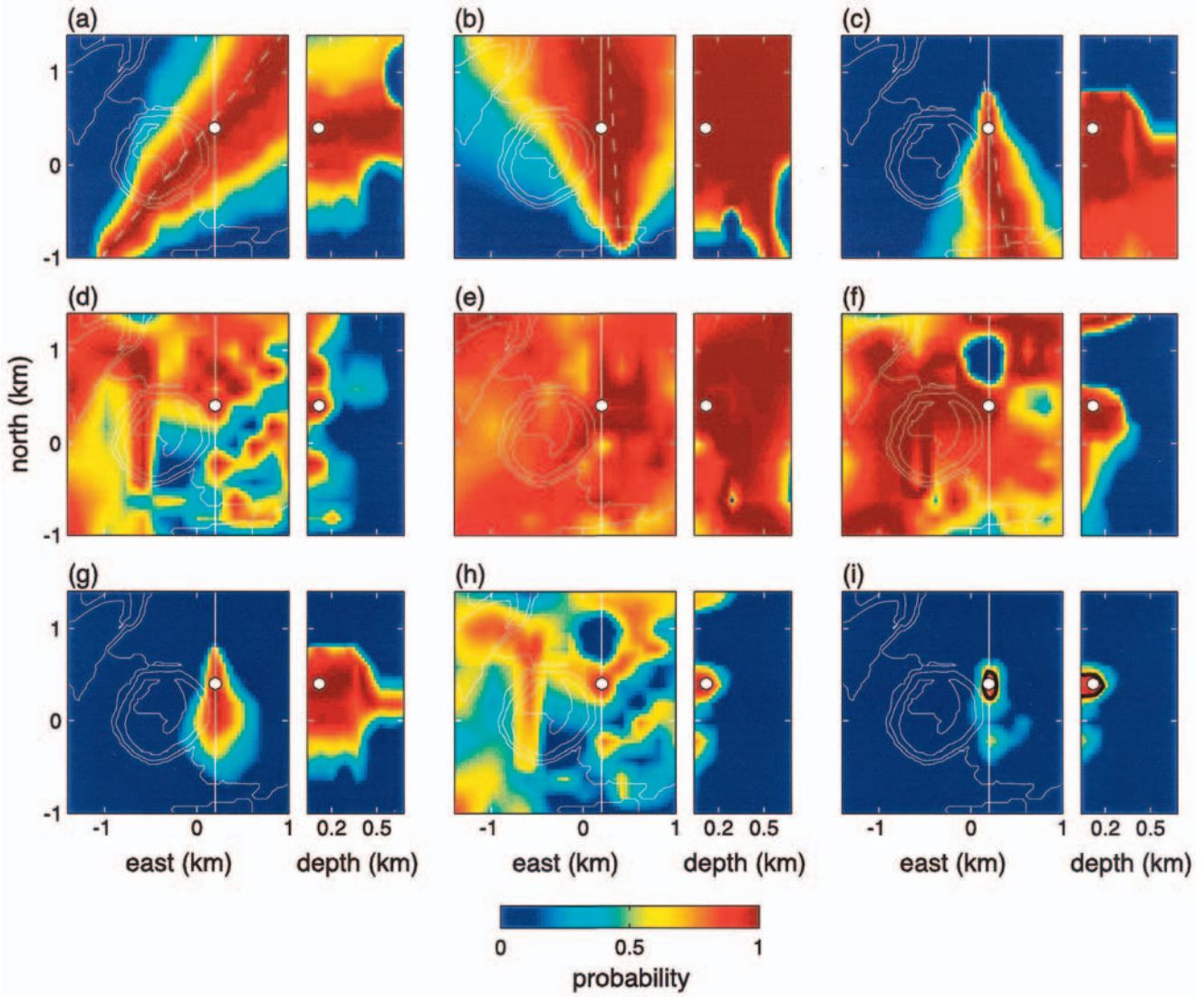

Plate 4. Map views of the shallowest layer in the slowness model at depth of 40 m and north-south vertical cross section of the spatial probability distributions used in the source location procedure of a synthetic event (same event as in Plate 3). The white circle marks the source position. The vertical lines in the map views mark the positions of the vertical cross sections. (a, b, c) Probability distributions for azimuth obtained at arrays DS, ES, and FS. The dashed white lines show the directions of the average back azimuths of the waves seen at the arrays. (d, e, f) Probability distributions for slowness obtained at arrays DS, ES, and FS. (g) Combined probability distribution for azimuth, the product of Plates 4a, 4b, and 4c. (h) Combined probability distribution for slowness, the product of Plates 4d, 4e, and 4f. (i) Spatial source probability distribution, which includes both azimuth and slowness information. The solid black line is the contour at 80% of the maximum probability, which we take as a measure of the error in the solution.

with the original source location. We use the slowness vector obtained for the synthetic event whose location is shown in Plate 4 and generate a set of 250 noisy slowness vectors by adding random noise with standard deviations of 5° in azimuth and 0.05 s/km in slowness. We then apply our location method using these noisy slowness vectors and find that the recalculated hypocenters are clustered around the original source location with a standard deviation of 125 m, which fits well within the error region that we are considering. This demonstrates that the source location procedure is stable. The location quality, however, is sensitive to small errors in the data and decays from 1.0 for the original source considered to an average of 0.7 for the ensemble of 250 noisy samples.

7.3. Dependence on the Choice of the Probability Distributions

An alternate choice of probability functions used in the calculation of the source location probability (equations (11) and (12)) has only a small effect on the resulting source locations. We test this dependence by using the triangular probability distributions shown by the dotted curves in Figure 2 and defined as

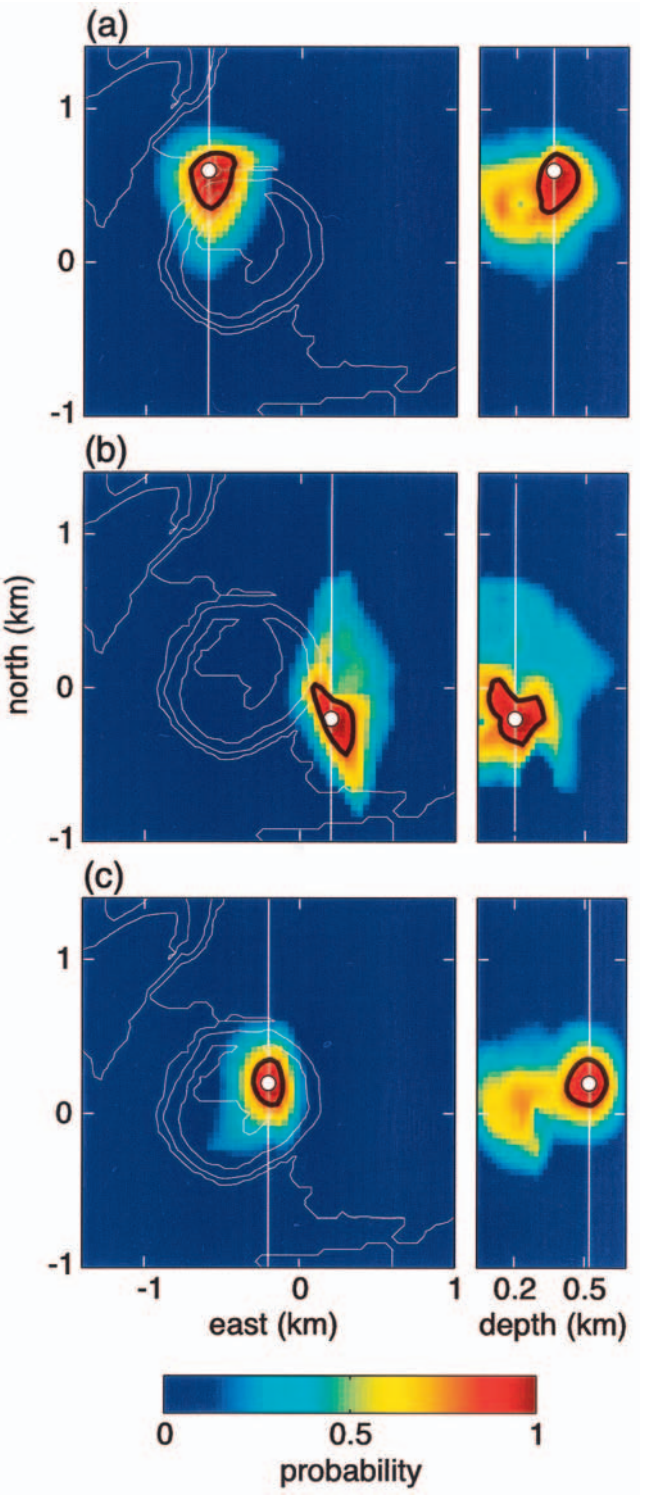

Plate 5. Same as Plate 4i for synthetic sources located at different positions in the domain. A white circle marks the original source location. The map views represent horizontal sections of the source location probability distributions at the source depth, as indicated by the white lines in the vertical cross sections. (a) Synthetic source located at coordinates (−600, 600, 360) m. (b) Synthetic source located at coordinates (200, −200, 200) m. (c) Synthetic source located at coordinates (−200, 200, 520) m. In each case the solution matches the original source position with a location quality close to 1.

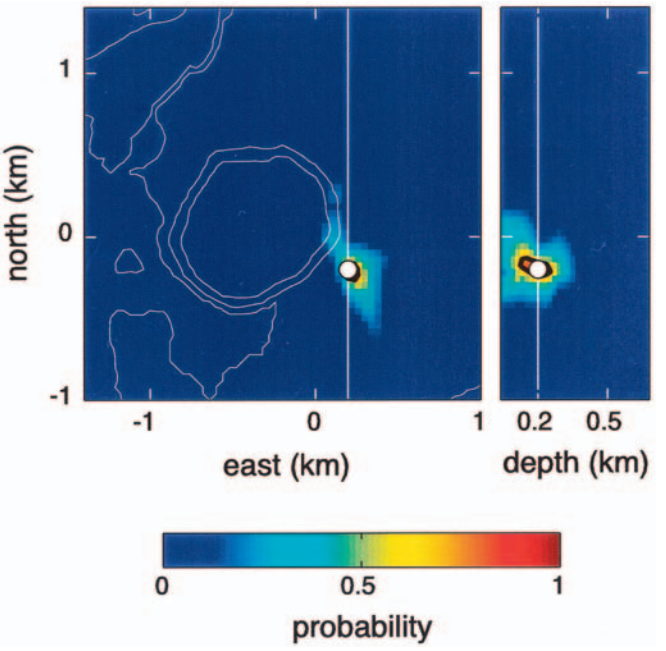

Plate 6. Same as Plate 5b for the spatial source probability distribution obtained using the alternate triangular probability distributions defined by (17) and (18). The solution matches the original position, but the location quality and the error region are different.

$$P_\phi^A(x, y, z) = \begin{cases} 0 & |\phi^A - \bar{\phi}_0^A| \geq \Delta\bar{\phi}^A, \\ 1 - \left| \dfrac{\phi^A(x, y, z) - \bar{\phi}_0^A}{\Delta\bar{\phi}^A} \right| & |\phi^A - \bar{\phi}_0^A| < \Delta\bar{\phi}^A, \end{cases} \tag{17}$$

$$P_s^A(x, y, z) = 0 \qquad s^A \leq \bar{s}_{\min}^A \text{ or } s^A \geq \bar{s}_{\max}^A, \tag{18a}$$

$$P_s^A(x, y, z) = 1 - \left| \frac{\bar{s}_0^A - s^A(x, y, z)}{\bar{s}_0^A - \bar{s}_{\min}^A} \right| \qquad \bar{s}_{\min}^A < s^A \leq \bar{s}_0^A, \tag{18b}$$

$$P_s^A(x, y, z) = 1 - \left| \frac{\bar{s}_0^A - s^A(x, y, z)}{\bar{s}_0^A - \bar{s}_{\max}^A} \right| \qquad \bar{s}_0^A < s^A < \bar{s}_{\max}^A, \tag{18c}$$

where $\Delta\bar{\phi}^A = \bar{\phi}_{\max}^A - \bar{\phi}_{\min}^A$. Plate 6 shows the location of the synthetic event in Plate 5b obtained using these triangular probability distributions. The only changes in the solution are differences in the relative weight between the probabilities obtained at different points of the domain, so that the location quality and overall smoothing of the picture are different. In particular, the error limits associated with the sharper triangular distributions appear quite small and unrealistic. In spite of these effects, the source locations derived with the triangular distributions are the same, within a few nodes, as those obtained previously with the Gaussian and Poissonian distributions. Thus we may conclude that the source locations are relatively independent of the choice of probability functions, as long as these functions satisfy the criteria defined in section 3.

8. Conclusions

We have presented a method designed to provide an estimate of the source position based on results from a standard frequency-slowness analysis of array data from at least two antennas. The source coordinates are obtained in a probabi-

listic sense by comparing the slowness vector data to a slowness vector model. The use of a restricted geometric slowness vector model may constitute a trade-off solution when the structure of the medium is not well known. If desired, information about the apparent slowness may be included in the model by using a simple homogeneous or layered medium. However, when information about the 3-D velocity structure is available, it is more appropriate to use a synthetic slowness vector model that takes into account the effects of topography and velocity structure to simulate the behavior of the propagating wave fields. Using a synthetic slowness vector model appropriate for the summit region of Kilauea caldera, along with a configuration of three seismic antennas similar to those deployed during a seismic experiment conducted in February 1997 [*Almendros et al*., this issue], we show that the source position can be estimated within an error of ± 200 m. We also demonstrate through a series of tests that the results obtained with our location method are reliable and that the effects of the limited resolution of the synthetic slowness vector model and of small errors in the data, as well as the effects resulting from our choice of different probability functions for azimuth and slowness, fall within the estimated location errors and do not significantly affect source locations.

Our results demonstrate that there is a bias in the epicenter position derived from the restricted geometric model, as compared to the hypocenter location derived from the synthetic model. The difference may amount up to 500 m and is caused by the effects of topography and lateral velocity heterogeneity. These effects can produce noticeable variations in the direction of the apparent slowness vector, which may deviate by up to 10° from the source-receiver azimuth. Improvements in the procedure, via the introduction of velocity models with better spatial resolution that will allow the calculation of synthetics to higher frequencies, will no doubt show that these effects are even more pronounced. However, for many applications the geometric model may be good enough. For example, a simple geometric model may be used to gain information about the source location for some signals that are otherwise elusive, such as coherent scattered waves present in the coda.

The initial determination of a synthetic slowness vector model requires extensive computations. However, once the model is established, it can be used to locate events recorded at seismic antennas with the same confidence that one uses a velocity model to determine earthquake hypocenters with a seismic network.

The successful application of a method based on a synthetic model is dependent upon our knowledge of the medium. A high-resolution tomographic model is required to generate synthetic seismograms that can reproduce to some level of accuracy the behavior of the wave fields observed in the medium. In the work presented here, we used a model interpolated from the 500-m spatial resolution tomography model determined for Kilauea by *Dawson et al*. [1999]. This model probably constitutes the most precise elaboration of the 3-D velocity structure of Kilauea today. This requirement, together with the high number of seismometers required to deploy even a few good quality small-aperture antennas, is the main difficulty that will need to be surmounted for a generalized application of the method.

Acknowledgments. We are grateful to Robert Page, Chris Stephens, Gaetano De Luca, Jesús Ibáñez, and Alan Linde for constructive comments. The work by J. Almendros was supported by a Fellowship of the Spanish Ministry of Education.

References

Almendros, J., J. M. Ibáñez, G. Alguacil, and E. Del Pezzo, Array analysis using circular wave-front geometry: An application to locate the nearby seismo-volcanic source, *Geophys. J. Int*., *136*, 159–170, 1999.

Almendros, J., J. M. Ibáñez, E. Del Pezzo, R. Ortiz, G. Alguacil, M. La Rocca, M. J. Blanco, and J. Morales, A seismic antenna survey at Teide Volcano: Evidences of local seismicity and inferences from non-existence of volcanic tremor, *J. Volcanol. Geotherm. Res*., *103*, 439–462, 2000.

Almendros, J., B. Chouet, and P. Dawson, Spatial extent of a hydrothermal system at Kilauea Volcano, Hawaii, determined from array analyses of shallow long-period seismicity, 2, Results, *J. Geophys. Res*., this issue.

Bratt, S., and T. Bache, Locating events with a sparse network of regional arrays, *Bull. Seismol. Soc. Am*., *78*, 780–798, 1988.

Capon, J., High-resolution frequency-wavenumber spectrum analysis, *Proc. IEEE*, *57*, 1408–1418, 1969.

Chouet, B., Long-period volcano seismicity: Its source and use in eruption forecasting, *Nature*, *380*, 309–316, 1996a.

Chouet, B., New methods and future trends in seismological volcano monitoring, in *Monitoring and Mitigation of Volcano Hazards*, edited by R. Scarpa and R. Tilling, pp. 23–97, Springer-Verlag, New York, 1996b.

Chouet, B., G. Saccorotti, M. Martini, P. Dawson, G. De Luca, G. Milana, and R. Scarpa, Source and path effects in the wave fields of tremor and explosions at Stromboli Volcano, Italy, *J. Geophys. Res*., *102*, 15,129–15,150, 1997.

Dawson, P., B. Chouet, P. Okubo, A. Villaseñor, and H. Benz, Three-dimensional velocity structure of the Kilauea caldera, Hawaii, *Geophys. Res. Lett*., *26*, 2805–2808, 1999.

Del Pezzo, E., M. La Rocca, and J. M. Ibáñez, Observations of high-frequency scattered waves using dense arrays at Teide volcano, *Bull. Seismol. Soc. Am*., *87*, 1637–1647, 1997.

Frankel, A., S. Hough, P. Friberg, and R. Busby, Observations of Loma Prieta aftershocks from a dense array in Sunnyvale, California, *Bull. Seismol. Soc. Am*., *81*, 1900–1922, 1991.

Goldstein, P., and R. Archuleta, Array analysis of seismic signals, *Geophys. Res. Lett*., *14*, 13–16, 1987.

Goldstein, P., and R. Archuleta, Deterministic frequency-wavenumber methods and direct measurements of rupture propagation during earthquakes using a dense array: Theory and methods, *J. Geophys. Res*., *96*, 6173–6185, 1991.

Goldstein, P., and B. Chouet, Array measurements and modeling of sources of shallow volcanic tremor at Kilauea Volcano, Hawaii, *J. Geophys. Res*., *99*, 2637–2652, 1994.

Ibáñez, J. M., J. Almendros, G. Alguacil, E. Del Pezzo, M. La Rocca, R. Ortiz, and A. García, Seismo-volcanic signals at Deception Island volcano (Antarctica): Wave field analysis and source modeling, *J. Geophys. Res*., *105*, 13,905–13,931, 2000.

Koyanagi, R. Y., B. Chouet, and K. Aki, Origin of volcanic tremor in Hawaii, part I, in *Volcanism in Hawaii*, edited by R. W. Decker, T. L. Wright, and P. H. Stauffer, *U.S. Geol. Surv. Prof. Pap*., *1350*, 1221–1257, 1987.

LaCoss, R. T., E. J. Kelly, and M. N. Toksöz, Estimation of seismic noise structure using arrays, *Geophysics*, *34*, 21–38, 1969.

Lahr, J. C., B. A. Chouet, C. D. Stephens, J. A. Power, and R. A. Page, Earthquake classification, location and error analysis in a volcanic environment: Implications for the magmatic system of the 1989–1990 eruptions at Redoubt Volcano, Alaska, *J. Volcanol. Geotherm. Res*., *62*, 137–151, 1994.

La Rocca, M., S. Petrosino, G. Saccorotti, M. Simini, J. Ibáñez, J. Almendros, and E. Del Pezzo, Location of the source and shallow velocity model deduced from the explosion quakes recorded by two seismic antennas at Stromboli Volcano, *Phys. Chem. Earth*, *25*, 731–736, 2000.

Métaxian, J. P., P. Lesage, and J. Dorel, Permanent tremor of Masaya volcano, Nicaragua: Wave field analysis and source location, *J. Geophys. Res*., *102*, 22,529–22,545, 1997.

Nafe, J. E., and C. L. Drake, Physical properties of marine sediments, in *The Sea*, vol. 3, *The Earth Beneath the Sea*, edited by M. N. Hill, pp. 794–815, Wiley-Interscience, New York, 1963.

Ohminato, T., and B. Chouet, A free-surface boundary condition for including 3D topography in the finite-difference method, *Bull. Seismol. Soc. Am*., *87*, 494–515, 1997.

Okubo, P. G., H. M. Benz, and B. A. Chouet, Imaging the crustal magma source beneath Mauna Loa and Kilauea volcanoes, Hawaii, *Geology*, *25*, 867–870, 1997.

Saccorotti, G., B. Chouet, M. Martini, and R. Scarpa, Bayesian statistics applied to the location of the source of explosions at Stromboli Volcano, Italy, *Bull. Seismol. Soc. Am*., *88*, 1099–1111, 1998.

Schmidt, R. O., Multiple emitter location and signal parameter estimation, *IEEE Trans. Antennas Propag*., *34*, 276–280, 1986.

Spudich, P., and D. Oppenheimer, Dense seismograph array observations of earthquake rupture dynamics, in *Earthquake Source Mechanism*, *Geophys. Monogr. Ser*., vol. 37, edited by S. Das, J. Boatwright, and C. Scholz, pp. 285–296, AGU, Washington, D. C., 1986.

Wang, H., and M. Kaveh, Coherent signal-subspace processing for the detection and estimation of angles of arrival of multiple wide-band source, *IEEE Trans. Acoust. Speech Signal Processes*, *33*, 823–831, 1985.

J. Almendros, B. Chouet, and P. Dawson, U.S. Geological Survey, 345 Middlefield Road, MS 910, Menlo Park, CA 94025. (noba@usgs.gov)

(Received September 26, 2000; revised March 2, 2001; accepted March 15, 2001.)